

Learning Local-Global Contextual Adaptation for Fully End-to-End Bottom-Up Human Pose Estimation

Nan Xue¹Tianfu Wu²Zhen Zhang¹Gui-Song Xia¹

¹ School of Computer Science, Wuhan University, China
 {xuenan, zhen-zhang, gui-song.xia}@whu.edu.cn

² Department of ECE, North Carolina State University, USA
 tianfu.wu@ncsu.edu

Abstract

This paper presents a method of learning *Local-Global* Contextual Adaptation for fully end-to-end and fast bottom-up human *Pose* estimation, dubbed as *LOGO-CAP*. It is built on the conceptually simple center-offset formulation that lacks inaccuracy for pose estimation. When revisiting the bottom-up human pose estimation with the thought of “thinking, fast and slow” by D. Kahneman, we introduce a “slow keypointer” to remedy the lack of sufficient accuracy of the “fast keypointer”. In learning the “slow keypointer”, the proposed LOGO-CAP lifts the initial “fast” keypoints by offset predictions to keypoint expansion maps (KEMs) to counter their uncertainty in two modules. Firstly, the local KEMs (e.g. 11×11) are extracted from a low-dimensional feature map. A proposed convolutional message passing module learns to “re-focus” the local KEMs to the keypoint attraction maps (KAMs) by accounting for the structured output prediction nature of human pose estimation, which is directly supervised by the object keypoint similarity (OKS) loss in training. Secondly, the global KEMs are extracted, with a sufficiently large region-of-interest (e.g., 97×97), from the keypoint heatmaps that are computed by a direct map-to-map regression. Then, a local-global contextual adaptation module is proposed to convolve the global KEMs using the learned KAMs as the kernels. This convolution can be understood as the learnable offsets guided deformable and dynamic convolution in a pose-sensitive way. The proposed method is end-to-end trainable with near real-time inference speed, obtaining state-of-the-art performance on the COCO keypoint benchmark for bottom-up human pose estimation. With the COCO trained model, our LOGO-CAP also outperforms prior arts by a large margin on the challenging OCHuman dataset.

1 Introduction

1.1 Motivation and Objective

Human pose is highly articulated with large structural and appearance variations. 2D human pose estimation in images is a classic structured output prediction problem, and remains a challenging one in computer vision and machine learning. Human pose estimation has numerous applications such as people-centered image understanding, autonomous driving and Augmented Reality (AR). With the recent resurgence of deep neural networks (DNNs), the performance of human pose estimation has witnessed remarkable improvement [12, 3, 17, 25, 11]. This paper focuses on the deep learning based problem formulation.

There are two deep learning based paradigms for human pose estimation in the literature. The top-down paradigm consists of human detection and single human pose estimation in each detected

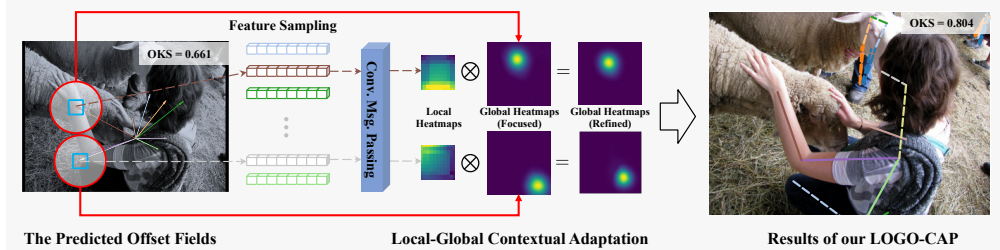


Figure 1: Illustration of the proposed LOGO-CAP for bottom-up human pose estimation. It is built on the center-offset representation. See text for detail.

human bounding box [12]. The bottom-up paradigm also includes two components: human pose keypoint detection and keypoint grouping [3]. The top-down paradigm often obtains better accuracy performance, but suffers from its inferior efficiency since the computational cost of the single human pose estimation component is linearly scaled with respect to the number of detected human bounding boxes in an image. It is also largely affected by the performance of the human detection component (e.g., not handling occlusion very well). Thanks to its efficiency, especially in real-time applications, the bottom-up paradigm becomes more and more attractive. For both paradigms, state-of-the-art methods often are not fully end-to-end trained and utilize different post-hoc processing modules to improve the performance. This paper is interested in developing a fully end-to-end bottom-up paradigm and aims at bridging its performance gap with the top-down paradigm.

For the bottom-up paradigm, the recently proposed center-offset approach [6, 31, 29, 11] is a conceptually simple formulation (see the left of Fig. 1 for an illustrative example and Fig. 3 for the detailed workflow). It alleviates the need of sophisticated keypoint grouping. When introducing human keypoints centers (i.e., anchors) by treating objects as points [39], it encodes a human pose as a star structure using the offset vectors of human keypoints relative to the anchors. The main challenge of the center-offset regression paradigm lies in the difficulty of accurately learning offset vectors with large structural variations, especially the long-range ones, which also leads to inferior performance. This paper builds on the center-offset approach and addresses its drawback.

1.2 Method Overview

To address the drawback of the center-offset formulation, we build the intuitive idea of “**Keypointing, fast and slow**”, by analogy to the modes of thought suggested by Daniel Kahneman in “*Thinking, fast and slow*” [15]: (i) *Fast Keypointer*: We treat the vanilla center-offset based estimation [39] as the *Fast Initializer* of pose estimation. (ii) *Slow Keypointer*: The lack of localization accuracy in the Fast Initializer entails a *Slow Solver* that learns to refine the “fast” keypoints. By slow, it is only relatively speaking. The Slow Keypointer is actually fast with near real-time speed.

To realize the Slow Keypointer, as illustrated in Fig. 1 and Fig. 3, this paper presents a method of learning **LOcal-GLObal Contextual Adaptation** for fully end-to-end and fast bottom-up human Pose estimation, dubbed as **LOGO-CAP**. To quantitatively motivate the proposed method, we first present a surprisingly strong observation for a vanilla center-offset regression method (Table 1) in the fully-annotated subset of the COCO val-2017 dataset. Specifically, the vanilla regression method utilizes the HRNet-W32 [30] as the feature backbone to directly predict keypoints center heatmap and the offset vectors. This vanilla center-offset model obtains 60.1 average precision (AP), which is not great, but reasonably good. It clearly shows that the pose keypoints center and the offset vectors can be learned reasonably well. Instead of directly utilizing the learned offset vectors for human pose estimation, we treat them as human pose keypoint initialization and do a local window search to compute the empirical upper-bound of performance. More detailed, based on the predicted human poses, by introducing a local window (e.g., 11×11) centered at each detected key point and by computing the single keypoint similarity with the ground-truth keypoint, an empirical upper-bound of 88.9 AP is obtained, which is significantly higher than the state of the art and shows the potential of improving the vanilla center-offset regression paradigm.

Table 1: The performance of a vanilla center-offset regression approach, its empirical upper bound, and the performance of our proposed LOGO-CAP using HRNet-W32 [30] as the feature backbone. See text for detail.

	Baseline	Emp. Bound	LOGO-CAP
AP	60.1	88.9	70.0
AP ⁵⁰	85.2	93.1	88.2
AP ⁷⁵	66.7	90.6	76.4
AP ^M	53.7	87.7	64.4
AP ^L	71.5	90.2	78.4

Motivated by the above observation, a straightforward way is just to learn a local heatmap (e.g., 11×11) for each human pose keypoint based on the learned center and offset vectors, and then to compute the refined keypoints by taking $\arg \max$ within the local heatmap. Although appealing, this does not work as observed during our development of the LOGO-CAP. The underlying reason is easy to understand: if this can work, the original offset vector regression should work at the first place since no additional information is introduced through learning the local heatmap. We *hypothesize* that on the one hand, on top of the local heatmap, the structural relationship between different keypoints of a human pose needs to be taken into account, and on the other hand, the intrinsic uncertainty of the local information in a local heatmap needs to be resolved. The former is the key challenge of structured output prediction problems. Many message passing algorithms have been developed in the literature. The latter can not be addressed by simply increasing the local window size. It entails learning stronger local-global information interaction and adaptation.

Along with the two hypotheses, the proposed LOGO-CAP lifts the initial keypoints via the center-offset prediction to keypoint expansion maps (KEMs) to counter their lack of localization accuracy in two modules (Section 3.2). The KEMs extend the star-structured representation of the center-offset formulation to the pictorial structure representation [10, 8]. The first module computes local KEMs and learns to account for the structured output prediction nature of the human pose estimation problem, leading to the keypoint attraction maps (KAMs). The second computes global KEMs and learns to refine the global KEMs by leveraging the KAMs.

Our LOGO-CAP is a fully end-to-end bottom-up human pose estimation method with near real-time inference speed. It obtains 70.0 AP in the fully-annotated subset of the COCO val-2017 dataset, which is an absolute increase of 9.9 AP compared to the vanilla center-offset method, making a significant step forward. Fig. 1 shows a pose estimation example. Fig. 2 shows the advantage of the proposed LOGO-CAP in terms of overall speed-accuracy comparisons between our LOGO-CAP and prior arts. Meanwhile, we should notice that there is also a significant gap compared to the empirical upper bound (Table 1), which encourages more work to be investigated.

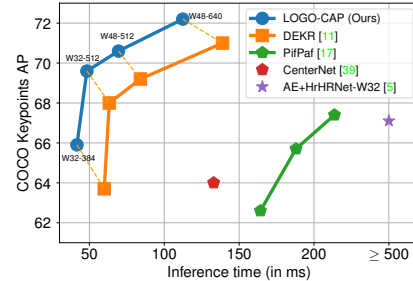


Figure 2: Speed-accuracy comparisons between our LOGO-CAP and prior arts on the COCO val-2017 dataset. Wx - Y (e.g. W32-384) means that a model uses the backbone HRNet- Wx (HRNet-W32) and is tested with the image resolution Y in the short side.

2 Related Works and Our Contributions

There is a vast body of literature for human pose estimation. Many elegant representation schema have been developed for modeling articulated human pose in the traditional approaches such as the well-known pictorial structure model [10, 8] and its many variants [27, 1, 26, 36, 28]. Most of them focused on single person pose estimation. They perform inference over a combination of local observations on body parts (i.e., the data term) and the spatial dependencies between them (i.e., the spring or clique term). The spatial dependencies are captured either using directed and acyclic structures that facilitate the global optimization by dynamic programming [2, 9], or using structures with loop introduced (for high-order part relationship modeling) which resort to approximate inference by loopy belief propagation [21]. The bottleneck of the traditional methods lies in the data term which is often based on hand-crafted features. With the resurgence of DNNs and the end-to-end learning, the data term has been largely improved. We briefly review the recent deep learning based approaches for bottom-up human pose estimation.

Limb-based Grouping Approaches have been extensively developed due to the naturalness of modeling limbs based on keypoints. Given a predefined limb configuration (e.g., the COCO person skeleton template consisting of 19 limbs based on 17 keypoints), the grouping can be addressed by Part affinity field (PAF) [4, 3], Associative Embedding (AE) [22], mid-range offset fields in Person-Lab [25] and the fields of Part Intensity and Association [17]. Typically, sophisticated designs are entailed to achieve good performance. For example, a bipartite graph matching is used in Open-Pose [3]. In addition to be computationally expensive, another drawback of these methods is not fully end-to-end trainable. More recently, the differentiability issue was studied by the Hierarchical Graph Clustering (HGG) method [14], which utilizes graph convolution networks to repeatedly delineate pose parameters of multiple persons from a keypoint graph. HGG improves the performance

compared to its baseline, the Associative Embedding method [22] at the expense of significantly increased computational cost. In contrast to those approaches, our proposed LOGO-CAP is fully end-to-end trainable and achieves near real-time inference speed.

Direct Regression based Approaches have attracted much attention due to their conceptually simple formulation [6, 31, 29, 11, 33]. These center-offset based formulations are inspired by the recent remarkable success of direct bounding box regression in object detection such as the FCOS method [32] and CenterNets [39, 6]. As aforementioned, one main challenge is the difficulty of accurately regress the offset vectors, especially for the long-range keypoints with respect to the center. Sophisticated post-processing schema are often entailed to improve the performance. For example, a method of matching the directly regressed poses to the nearest keypoints that are extracted from the global keypoint heatmaps is used in [39]. Although being simple, the performance of this line of work is usually inferior to the limb-based approaches. The mixture regression network [33] alleviated the issue of regression quality to some extent, but still remained an indispensable performance gap comparing with the grouping-based approaches. Most recently, Geng *et al.* presented the first competitive direct method, DEKR [11] with a novel pose-specific neural architecture for disentangled keypoint regression. To improve the performance, the DEKR method utilizes a lightweight rescoring network to recalibrate the pose scores that are computed based on the keypoint heatmaps. Despite good performance, the DEKR method entails the additional rescoring stage in both training and testing, and thus is not fully end-to-end. The proposed LOGO-CAP retains the simplicity of the vanilla center-offset formulation and enjoys fully end-to-end training and fast inference speed.

Our Contributions. The proposed LOGO-CAP makes three main contributions to the field of bottom-up human pose estimation: (i) It addresses the drawback of the vanilla center-offset formulation while retaining its efficiency. It proposes the key idea of lifting a keypoint to a keypoint expansion map to counter the lack of localization accuracy. It is fully end-to-end trainable, unlike many other bottom-up human pose estimation methods which entail separate post-hoc processing to improve performance. (ii) It presents a novel local-global contextual adaptation formulation that accounts for the nature of structured output prediction in human pose estimation and harnesses local-global structural information integration. (iii) It obtains state-of-the-art performance in the COCO val-2017 and test-2017 datasets. It also shows state-of-the-art transferability performance in the OCHuman dataset.

3 Approach

3.1 Problem Formulation

We follow the COCO protocol of defining the human pose. It consists of 17 human pose keypoints: 8 pairs of symmetric keypoints (hips, ankles, knees, shoulders, elbows, wrists, ears and eyes) and the nose keypoint. Let $P = \{1, \dots, 17\}$ be the set of keypoint indexes using a predefined order. Let Λ be an image lattice of the spatial size $H \times W$ (e.g., 512×512), and I be an image defined on Λ . Let P_I^n be the set of keypoint indexes for a human pose instance n in an image I and we have $P_I^n \subseteq P$. For example, in COCO, we typically have $1 \leq n \leq 30$, and different human pose instances have different number of visible keypoints due to occlusion and/or truncation. Denote by $L_I^n = \{(x_i, y_i); i \in P_I^n\}$ the keypoint locations of a human pose instance n in an image I , where $(x_i, y_i) \in \Lambda$. In the center-offset formulation, we introduce the keypoints center (i.e., the anchor), (x_c, y_c) based on a given L_I^n and we have,

$$x_c = 1/|L_I^n| \cdot \sum_{i \in P_I^n} x_i, \quad y_c = 1/|L_I^n| \cdot \sum_{i \in P_I^n} y_i. \quad (1)$$

With the anchor, a keypoint (x_i, y_i) is equivalently defined by its offset/displacement, denoted by $(\Delta x_i, \Delta y_i)$ with $\Delta x_i = x_i - x_c$ and $\Delta y_i = y_i - y_c$. So, L_I^n can also be equivalently expressed as $L_I^n = \{(x_c, y_c), (\Delta x_i, \Delta y_i); i \in P_I^n\}$.

The objective of human pose estimation is to recover $L_I^n = \{(x_i, y_i); i \in P_I^n\}$ for all human pose instances in an image. Denote by $\hat{L}_I^n = \{(\hat{x}_i, \hat{y}_i); i \in P_I^n\}$ the estimated human pose. Following the COCO protocol, the object keypoint similarity (OKS) is used to evaluate the accuracy,

$$\ell_{OKS}(\hat{L}_I^n, L_I^n) = 1/|P_I^n| \cdot \sum_{i \in P_I^n} \exp(-d_i^2/2s^2\kappa_i^2), \quad (2)$$

where d_i is the Euclidian distance between the ground-truth keypoint (x_i, y_i) and the predicted one (\hat{x}_i, \hat{y}_i) . s is the square root of the human segment area, and κ per-keypoint constant that controls fall-off in evaluation. We have $\ell_{OKS}(\hat{L}_I^n, L_I^n) \in [0, 1]$. The OKS metric is to evaluate the distance

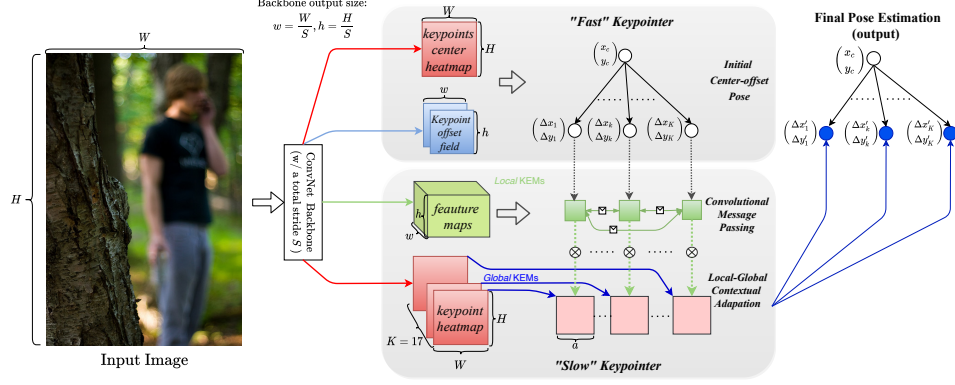


Figure 3: Illustration of the network and algorithmic flow of the proposed LOGO-CAP for bottom-up human pose estimation. See text for detail.

between predicted keypoints and ground-truth keypoints normalized by the scale of the person with the importance of keypoints equalized. In benchmarking different methods, the average precision (AP) at OKS= 0.50 : 0.05 : 0.95 is used as the primary metric, together with AP^{50} at OKS= 0.50, AP^{75} at OKS= 0.75, and AP across medium and large scales, AP^M and AP^L respectively.

3.2 The Proposed LOGO-CAP

We first present the network and the inference of LOGO-CAP, and then give details of the training. We keep different modules of the proposed LOGO-CAP simple, which in turn highlights the effectiveness of the proposed representation and algorithmic flow.

3.2.1 The Network and the Inference

As illustrated in Fig. 3, the proposed LOGO-CAP consists of four components as follows.

i) A convolution neural network feature backbone. Given an input image I , the output of the feature backbone is a C -dim feature map, denoted by $F \in R^{C \times h \times w}$, where C is the feature dimension of the last convolutional layer in the feature backbone, and the spatial size $h \times w$ depends on the total stride in the feature backbone. We use off-the-shelf HRNets [30] in our experiments.

ii) A parallel keypoint-offset regression module. Given the feature map F , the output of keypoint regression is an 18-dim feature map (i.e., heatmaps) for the 17 keypoints and the keypoints center respectively. Denote by $\mathcal{H} \in R^{18 \times h \times w}$ the heatmaps, and by $\mathcal{H}^\uparrow \in R^{18 \times H \times W}$ the up-sampled heatmaps (using bi-linear interpolation in our experiments). The output of offset regression is a 34-dim feature map (i.e., the offset vector fields) for the 17 keypoints. Denote by $\mathcal{O} \in R^{34 \times h \times w}$ the offset fields. We adopt a minimally-simple design in realizing the regression modules using a channel-wise multi-layer perceptron (MLP). In implementation, we first apply dimension reduction to the feature map F using a 1×1 convolution followed by a Batch Normalization (BN) and a Rectified Linear Unit (ReLU). Then, the output is computed by a 1×1 convolution. More specifically, we have the two parallel branches as follows,

$$F_{C \times h \times w} \xrightarrow[C \times 1 \times 1 \times C_1]{Conv+BN+ReLU} F_{C_1 \times h \times w}^{\mathcal{H}} \xrightarrow[C_1 \times 1 \times 1 \times 18]{Conv} \mathcal{H}_{18 \times h \times w} \xrightarrow[\text{bi-linear}]{UpSampling} \mathcal{H}_{18 \times H \times W}^\uparrow, \quad (3)$$

$$F_{C \times h \times w} \xrightarrow[C \times 1 \times 1 \times C_2]{Conv+BN+ReLU} F_{C_2 \times h \times w}^{\mathcal{O}} \xrightarrow[C_2 \times 1 \times 1 \times 34]{Conv} \mathcal{O}_{34 \times h \times w}, \quad (4)$$

where C_1 and C_2 are predefined (e.g., $C_1 = 32$ and $C_2 = 256$ are typically used).

Initial pose estimation via the center-offset approach. Based on the computed keypoints center heatmap $\mathcal{H}_{(18)}^\uparrow$ and offset fields \mathcal{O} , a predefined maximum number of pose candidates is computed as done in the vanilla center-offset approach. A non-maximum suppression (NMS) with a 3×3 window is applied in $\mathcal{H}_{(18)}^\uparrow$ and then the top- N keypoints centers are selected (e.g., $N = 30$ in our experiments). The N pose instances are computed by retrieving their offset vectors in \mathcal{O} based on the selected N keypoints centers. The N pose instances are further pruned by thresholding their confidence scores in $\mathcal{H}_{(18)}^\uparrow$ with a predefined threshold (e.g., 0.01 used in our experiments). Without confusion in the context, we still use N to denote the number of poses instances by this initial pose

estimation step. We obtain the set of estimated keypoints centers, denoted by $\mathcal{C}_{N \times 3}$ each row of which represents the position coordinates and the confidence score.

Lifting a keypoint to a keypoint expansion map (KEM) by imposing a mesh. For each of the N pose instances, each of the 17 keypoints are placed in a local geometric mesh (e.g., 11×11) with the estimated location as the mesh center, capturing the uncertainty of the center-offset pose estimation as aforementioned in the introduction. This mesh can thus be interpreted as keypoint expansion map (KEM), accounting for competency-aware representations. The entire mesh is denoted by $\mathcal{M}_{N \times 17 \times 11 \times 11 \times 2}$, which is used in computing the empirical upper bound in Table 1. We have,

$$\{\mathcal{H}_{(18)}^\uparrow, \mathcal{O}_{34 \times h \times w}\} \xrightarrow[\text{center-offset}]{\text{initial pose estimation}} \{\mathcal{C}_{N \times 3}, \mathcal{M}_{N \times 17 \times 11 \times 11 \times 2}\} \quad (5)$$

iii) A convolution message passing module. We first encode the geometric mesh $\mathcal{M}_{N \times 17 \times 11 \times 11 \times 2}$ in a latent space with the dimensionality C_3 (e.g., 64 in our experiments), computed based on the feature backbone output. Then, a keypoint is represented by a $C_3 \times 11 \times 11$ local feature map. A pose instance is represented by concatenating all the 17 keypoints. We have,

$$F_{C \times h \times w} \xrightarrow[C \times 1 \times 1 \times C_3]{\text{Conv+BN+ReLU}} F_{C_3 \times h \times w}^{\mathcal{M}} \xrightarrow[\text{bi-linear}]{\mathcal{M}_{N \times 17 \times 11 \times 11 \times 2}} \mathcal{K}_{N \times (17 \times C_3) \times 11 \times 11}, \quad (6)$$

where the bi-linear interpolation is used due to the sub-pixel based locations in the mesh and for better feature alignment.

To facilitate the structural information flow between different latent codes of the keypoints of a pose instance, we propose a simple convolutional message passing (CMP) module with three layers of Conv+BN+ReLU operations,

$$\mathcal{K}_{N \times (17 \times C_3) \times 11 \times 11} \Rightarrow \left[\frac{\text{Conv+BN+ReLU}}{C_{in} \times 3 \times 3 \times C_{out}} \right] \times 3 \Rightarrow \cdot \frac{\text{Conv}}{C_6 \times 1 \times 1 \times 17} \mathcal{K}_{N \times 17 \times 11 \times 11}, \quad (7)$$

where $C_{in} \in \{(17 \times C_3), C_4, C_5\}$ and $C_{out} \in \{C_4, C_5, C_6\}$ (e.g., $C_4 = 512, C_5 = 256, C_6 = 128$ in our experiments). The resulting $\mathcal{K}_{N \times 17 \times 11 \times 11}$ can be interpreted as keypoint attraction maps (KAMs) which are “re-focused” based on the KEMs by the CMP. To account for the specificity of different pose instances in the CMP, we adopt the Attention Normalization [19] to replace the BN in the second Conv+BN+ReLU layer, which further improves the performance in our experiments.

Through the CMP, we obtain the dynamic (a.k.a., data-driven) kernels for the 17 keypoints in a pose instance-sensitive way, which are used to refine the global heatmaps \mathcal{H}^\uparrow for the 17 keypoints.

iv) A local-global contextual adaptation module. We first compute another geometric mesh with enlarged mesh window $a \times a$ (e.g., $a = 97$) for each keypoint of the N pose instances, and the entire mesh is denoted by $\mathcal{M}_{N \times 17 \times a \times a \times 2}^L$, as done in Eqn. 5. The mesh can be interpreted as the global KEM. It is then instantiated with appearance features extracted from the global heatmaps $\mathcal{H}_{(1:17)}^\uparrow$, similar to Eqn. 6, and we have,

$$\mathcal{H}_{(1:17)}^\uparrow \xrightarrow[\text{bi-linear}]{\mathcal{M}_{N \times 17 \times a \times a \times 2}^L} \mathbb{H}_{N \times 17 \times a \times a} \xrightarrow[\text{reweighing}]{\mathcal{G}_{a \times a}(0, \sigma)} \tilde{\mathbb{H}}_{N \times 17 \times a \times a}. \quad (8)$$

where to encode the Gaussian prior of keypoint heatmaps, the resulting pose-guided heatmaps \mathbb{H} is reweighed by a Gaussian kernel $\mathcal{G}_{a \times a}(0, \sigma = \frac{a-1}{2 \times 3})$ (e.g., $\sigma = 16$ when $a = 97$) in an element-wise way. By doing so, it means that the enlarged mesh follows the 3σ principle.

Then, we apply the learned keypoint 11×11 kernels $K_{n,i}$ ’s (Eqn. 7) to convolve the reweighed $a \times a$ heatmap $\tilde{\mathbb{H}}_{n,i}$ (Eqn. 8) in a pose instance-sensitive and keypoint-specific way, leading to **Local-Global Contextual Adaptation**,

$$\tilde{\mathbb{H}}_{N \times 17 \times a \times a} \xrightarrow[\text{LOGO-CA}]{K_{N \times 17 \times 11 \times 11}} \tilde{\tilde{\mathbb{H}}}_{N \times 17 \times a \times a}, \quad (9)$$

which represents the refined heatmaps for the 17 human pose keypoints.

The Pose Estimation Output. With the local-global contextually adapted heatmaps $\tilde{\tilde{\mathbb{H}}}_{N \times 17 \times a \times a}$, we maintain the top-2 locations for each keypoint within the $a \times a$ heatmap, and then utilize a convex average of the top-2 locations as the final predicted offset vectors (i.e. $(\Delta x'_i, \Delta y'_i)$ ’s in Fig. 3), and of their confidence scores as the prediction score, with a predefined weight λ for the top-1 location (0.75 in our experiments). Together with the predicted keypoints centers $\mathcal{C}_{N \times 3}$ (Eqn. 5), the final prediction score for each keypoint is the product between the convex average confidence score and

the center confidence score. We keep the keypoints whose final scores are greater than 0. We have,

$$\{\mathcal{C}_{N \times 3}, \tilde{\mathbb{H}}_{N \times 17 \times a \times a}\} \xrightarrow[\text{Score thresholding}]{\text{Output}} \{\hat{L}_I^n; n = 1, \dots, N'\}, \quad (10)$$

where N' is the number of the final predicted pose instances in an image I .

3.2.2 Loss Functions in Training

In the fully end-to-end training, we need to define loss functions for the global heatmap \mathcal{H} (Eqn. 3), the refined local heatmap $\tilde{\mathbb{H}}$ (Eqn. 9), the offset field \mathcal{O} (Eqn. 4), and the keypoint kernels (Eqn. 7).

The Heatmap Loss. The widely adopted mean squared error (MSE) loss is used. Denoted by $\mathcal{H}_{18 \times h \times w}^{GT}$ the ground truth heatmaps in which each keypoint (including the center) is modeled by a 2-D Gaussian with dataset-provided mean and variance. Let $\mathbf{p} = (i, \mathbf{x})$ be the index of the domain D of dimensions $18 \times h \times w$. For the predicted heatmaps $\mathcal{H}_{18 \times h \times w}$, the MSE loss is defined by,

$$\mathcal{L}_{\mathcal{H}} = 1/|D| \cdot \sum_{\mathbf{p} \in D} \|w(\mathbf{x})(\mathcal{H}(\mathbf{p}) - \hat{\mathcal{H}}(\mathbf{p}))\|_2^2, \quad (11)$$

where $w(\mathbf{x})$ represents the weight for the foreground and the background pixels. The foreground mask is provided by the dataset annotation. In our experiment, we set $w(\mathbf{x}) = 1$ for a foreground pixel and $w(\mathbf{x}) = 0.1$ for a background pixel.

In defining the loss function $\mathcal{L}_{\tilde{\mathbb{H}}}$ for the refined local heatmap $\tilde{\mathbb{H}}$ (Eqn. 9), the ground-truth heatmap $\tilde{\mathbb{H}}^{GT}$ is generated on-the-fly based on the mesh $\mathcal{M}_{N \times 17 \times a \times a}^L$ (Eqn. 8) and the ground-truth keypoints using a Gaussian model with mean being the displacement between the current predicted keypoints and the ground-truth ones, and variance σ (i.e., the standard deviation of the reweighing Gaussian prior model in Eqn. 8).

The Offset Field Loss. The widely adopted SmoothL1 loss [] is used. Let $\mathcal{O}_{34 \times h \times w}^{GT}$ be the ground-truth offset field, and \mathcal{C}^{GT} be the non-empty set of ground-truth keypoints centers (Eqn. 1). For the predicted offset field $\mathcal{O}_{34 \times h \times w}$ (Eqn. 4), we have,

$$\mathcal{L}_{\mathcal{O}} = 1/|\mathcal{C}^{GT}| \cdot \sum_{\mathbf{p} \in \mathcal{C}^{GT}} \mathcal{A}(\mathbf{p}) \cdot \text{SmoothL1}(\mathcal{O}(\cdot, \mathbf{p}), \mathcal{O}^{GT}(\cdot, \mathbf{p}); \beta), \quad (12)$$

where $\mathcal{A}(\mathbf{p})$ is the area of the person centered at the pixel \mathbf{p} , and β the cutting-off threshold (e.g., $\frac{1}{9}$ in our experiments), and $\text{SmoothL1}(a, b; \beta) = 0.5 \times |a - b|^2 / \beta$ if $|a - b| \leq \beta$, otherwise $|a - b| - 0.5 \times \beta$.

The OKS Loss for the Keypoint Kernels. Consider a single predicted pose instance, learning the keypoint kernels, $K_{17 \times 11 \times 11}$ (Eqn. 7) is the key to facilitate the local-global contextual adaptation. To that end, the figure of merits of the KEF, $\mathcal{M}_{17 \times 11 \times 11 \times 2}$ (Eqn. 5) needs to directly reflect the task loss, i.e., the OKS loss (Eqn. 2). With respect to the N^{GT} ground-truth pose instances in an image, we can compute the similarity score per keypoint candidate in the KEF, and obtain the score tensor $S_{17 \times 11 \times 11 \times N^{GT}}$. The score tensor is further clamped with a threshold 0.5, i.e., $S_{17 \times 11 \times 11 \times N^{GT}} = \max(S_{17 \times 11 \times 11 \times N^{GT}}, 0.5)$. A mean reduction is applied to the first three dimensions of the clamped score tensor to compute the matching score for each of the N^{GT} pose instance. Then, the best ground-truth pose instance indexed by n^* is selected in terms of the matching score, and its matching score is denoted by s_{n^*} . Based on the selected ground-truth pose instance, we compute the per-keypoint similarity score for the predicted pose instance at hand, denoted by s_k ($k \in [1, 17]$). Then, the loss function for the keypoint kernels are defined by,

$$\mathcal{L}_K = s_{n^*} \cdot \sum_{k, i, j} s_k \cdot |K_{k, i, j} - S_{k, i, j, n^*}|^2. \quad (13)$$

The Total Loss is then defined by $\mathcal{L} = \mathcal{L}_{\mathcal{H}} + \mathcal{L}_{\tilde{\mathbb{H}}} + \lambda \cdot (\mathcal{L}_{\mathcal{O}} + \mathcal{L}_K)$, where the trade-off parameter λ is used to balance the different loss items ($\lambda = 0.01$ in our experiments).

4 Experiments

In this section, we present detailed experimental results and analyses of the proposed LOGO-CAP.

Datasets. We use two datasets in our experiments: **The COCO dataset [20]** is the most popular testbed for human pose estimation. It consists of 65k, 5k and 20k images with human pose well-annotated in the training, validation and testing datasets respectively. In all experiments, the proposed LOGO-CAP is trained using the 65k training images. **The OCHuman dataset [38]** is one popular *testing-only* dataset for evaluating human pose estimation under the occlusion scenarios. It

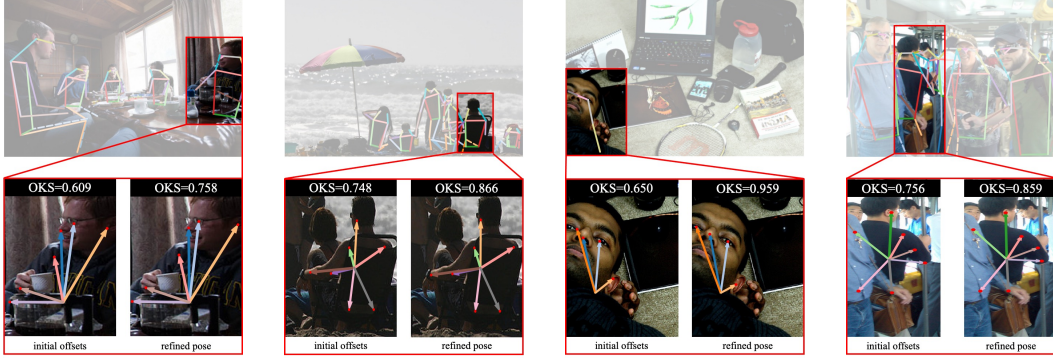


Figure 4: Examples of human pose estimation in the COCO val-2017 dataset by the proposed LOGO-CAP with the HRNet-W32 backbone. *Top*: The COCO skeleton template based visualization. *Bottom*: The close-up visualization and OKS comparisons between the initial center-offset estimation and the refined keypoints.

Table 2: Evaluation results on the COCO-val-2017 and COCO-testdev-2017 dataset. For HGG [14] and SimplePose [18], the multi-scale inference[†] is applied on the testdev-2017 dataset. For DEKR [11] that uses an rescoring network to get the final predictions, we report both the performance with and without rescoring (which is the fair baseline for our LOGO-CAP). The numbers of SPM [24] and HGG [14] are extracted from their papers.

	Method	Backbone	COCO-val-2017					COCO-testdev-2017				
			AP [%]	AP ⁵⁰ [%]	AP ⁷⁵ [%]	AP ^M [%]	AP ^L [%]	AP [%]	AP ⁵⁰ [%]	AP ⁷⁵ [%]	AP ^M [%]	AP ^L [%]
Grouping	OpenPose [39]	VGG-19	61.0	84.9	67.5	56.3	69.3	61.8	84.9	67.5	57.1	68.2
	PifPaf [17]	ResNet-152	67.4	86.9	73.8	63.1	74.1	66.7	87.8	73.6	62.4	72.9
	PersonLab [25]	ResNet-152	66.5	86.2	71.9	62.3	73.2	66.5	88.0	72.6	62.4	72.3
	AE [22, 5]	HrHRNet-W32	67.1	86.2	73.0	61.5	76.1	66.4	87.5	72.8	61.2	74.2
		HrHRNet-W48	69.9	87.2	76.1	65.4	76.4	68.4	88.2	75.1	64.4	74.2
	HGG [14]	Hourglass	60.4	83.0	66.2	—	—	67.6 [†]	85.1 [†]	73.7 [†]	62.7 [†]	74.6 [†]
	SimplePose [18]	IMHN	66.1	85.9	71.6	59.8	76.2	68.5 [†]	86.7 [†]	74.9 [†]	66.4 [†]	71.9 [†]
			—	—	—	—	—	66.9	88.5	72.9	62.6	0.731
Direct	CenterNet [39]	Hourglass	64.0	85.6	70.2	59.4	72.1	63.0	86.8	69.6	58.9	70.4
	DEKR [11]	HRNet-W32	68.0	86.7	74.5	62.1	77.7	67.3	87.9	74.1	61.5	76.1
		HRNet-W48	71.0	88.3	77.4	66.7	78.5	70.0	89.4	77.3	65.7	76.9
	DEKR [11]	HRNet-W32	67.2	86.3	73.8	61.7	77.1	66.6	87.6	73.5	61.2	75.6
		HRNet-W48	70.3	87.9	76.8	66.3	78.0	69.3	89.1	76.7	65.3	76.4
	LOGO-CAP (Ours)	HRNet-W32	69.6	87.5	75.9	64.1	78.0	68.2	88.7	74.9	62.8	76.0
		HRNet-W48	72.2	88.9	78.9	68.1	78.9	70.8	89.7	77.8	66.7	77.0

consists of a total number of 4713 images with 8110 detailed annotated human pose instances using the COCO keypoint configuration. All the annotated 8110 human pose instances have occlusions with the $\max\text{IOU} \geq 0.5$. Furthermore, 32% instances are more challenging with the $\max\text{IOU} \geq 0.75$.

4.1 Results on the COCO Dataset

Fig. 4 shows some qualitative examples of human pose estimation by the proposed LOGO-CAP. More examples will be provided in the supplementary material.

The proposed LOGO-CAP is compared with prior arts including OpenPose [3], PifPaf [17], PersonLab [25], AE [22] and DEKR [11]. As reported in Table 2, the proposed LOGO-CAP outperforms all of them on both both validation and test-dev datasets.

In comparisons to the best-performing grouping approach, AE [22] with a larger backbone HrHRNet-W48 [5], our LOGO-CAP obtains competitive performance with a smaller HRNet-32 backbone, and improves the AP score with HRNet-W48 backbone on the validation and testdev datasets by 2.3 and 2.5 points, respectively. For the fully differentiable grouping approach HGG [14], our LOGO-CAP achieves better performance by a significantly large margin, more than 9.2 points on the validation set under the single-scale testing. Although the performance of HGG is improved by the multi-scale testing on the test-dev set, the performance of our LOGO-CAP is still significantly better without using the multi-scale testing scheme.

In comparisons to the direct regression based approaches, our LOGO-CAP obtains the *best results* without incurring either the matching scheme used in CenterNet [39] or the additional rescoring network used in DEKR [11]. When we disable the rescoring network for DEKR [11] for fair com-

Table 3: Results on the OCHuman validation and testing datasets [38].

	Methods	Backbone	Val. AP [%]	Test AP [%]
Top-down	RMPE [7]	Hourglass	38.8	30.7
	SBL [35]	ResNet-50	37.8	30.4
	SBL [35]	ResNet-152	41.0	33.3
Bottom-up	AE [22]	Hourglass	32.1	29.5
	HGG [22]	Hourglass	35.6	34.8
	DEKR [11]	HRNet-W32	37.9	36.5
		HRNet-W48	38.8	38.2
	LOGO-CAP (Ours)	HRNet-W32	39.0	38.1
		HRNet-W48	41.2	40.4

Table 4: The single image inference speed comparison for bottom-up human pose estimation approaches.

Method	AP [%]	Backbone	Time ↓ [ms]	FPS ↑
PifPaf [17]	67.4	ResNet-152	213	4.68
AE [22, 5]	67.1	HrHRNet-W32	560	1.78
CenterNet [39]	64.0	Hourglass	147	6.80
DEKR [11]	68.0	HRNet-W32	63	15.8
DEKR [11]	71.0	HRNet-W48	139	7.21
LOGO-CAP	69.6	HRNet-W32	48	20.7
LOGO-CAP	72.2	HRNet-W48	112	8.95

parisons, our LOGO-CAP significantly improves the AP on the validation and testdev datasets by 2.4 points and 1.6 points respectively when HRNet-W32 is used as backbone. The larger backbone is beneficial for both DEKR and our method, which further improves the AP score of our LOGO-CAP to 72.2 and 70.8 on the validation and test-dev dataset respectively, outperforming DEKR by 1.9 and 1.5 respectively. Further detailed ablation studies are presented in Appendix B.

4.2 Results on the OCHuman Dataset

Table 3 shows that our LOGO-CAP achieves the best AP performance on both the validation and testing datasets by significant margins of 2.4 and 2.2 points in comparing with the bottom-up approaches. For the top-down approaches, although they obtain strong AP scores on the validation split, there exists a large performance gap between the validation and testing sets. In comparisons to DEKR [11] (with the rescoring network), our LOGO-CAP improves the performance from 37.9 to 39.0 and from 36.5 to 38.1 on the validation and testing splits with the same backbone HRNet-W32, respectively. The similar improvement is observed when the HRNet-W48 backbone is used, outperforming both bottom-up and top-down approaches.

4.3 Inference Speed

In comparing the inference speed, we test all the models on a single TITAN RTX GPU for its popularity in practice. The average inference speed, FPS (frames per second), over the 5000 images in COCO-val-2017 is used for the comparison. For DEKR [11], we re-implement their inference code with better speed obtained for fair comparisons at the algorithm level. For methods that have post-processing schema on CPU, only one thread is used. As shown in Table 4, our LOGO-CAP runs significantly faster than PifPaf [17] and AE [22]. The CenterNet [39] runs slower than DEKR and our LOGO-CAP as it requires a post-processing scheme to match the predicted offsets to the keypoints obtained from heatmaps. Comparing with DEKR, the speed improvement of our LOGO-CAP is from the lightweight design of head modules since the same backbones are used. For the comparisons in Table 2, we run the models with different resolutions of testing images.

4.4 Potentials and Limitations of the Proposed LOGO-CAP

Consider the generic applicability of the center-offset formulation to many computer vision tasks as demonstrated in [39], we hypothesize that the proposed LOGO-CAP has a great potential to remedy the lack of sufficient accuracy using the vanilla center-offset method in those tasks. We also notice that the minimally-simple design in learning the “Slow Keypointer” can be relaxed for different accuracy-speed trade-offs in practice. For example, for the convolutional message passing module, an alternative method could be the Transformer model [34], which potentially will further improve the performance at the expense of inference speed. We leave these for future work.

5 Conclusion

This paper focuses on deep learning based formulation for bottom-up human pose estimation. It presents a method of learning Local-Global Contextual Adaptation for Pose estimation, dubbed as LOGO-CAP. The proposed LOGO-CAP is built on the conceptually simple center-offset paradigm and addresses its drawback of lacking the capability of accurately localizing human pose keypoints. The key idea of our LOGO-CAP is to lift the center-offset predicted keypoints to keypoint expansion maps (KEMs), which counters the inaccuracy and uncertainty of the initial keypoints. Two types of KEMs are introduced in two parallel modules on top of the feature backbone. Local KEMs are used to learn keypoint attraction maps (KAMs) via a convolutional message passing module that accounts

for the structured output prediction nature of human pose estimation. Global KEMs are used to learn local-global contextual adaptation which convolves global KEMs using the KAMs as kernels. The refined global KEMs are used in computing the final human pose estimation. The proposed LOGO-CAP obtains state-of-the-art performance in COCO val-2017 and test-dev 2017 datasets for bottom-up human pose estimation. It also achieves state-of-the-art transferability performance in the OCHuman dataset with the COCO trained models.

Appendix

A Experimental Settings

Our PyTorch source code will be released. We briefly present the details of training and testing as follows.

Training. We train two LOGO-CAP networks with the ImageNet pretrained HRNet-W32 and HRNet-W48 [30] as the feature backbone respectively on the COCO-train-2017 dataset [20]. Common training specifications are used for simplicity in experiments. The Adam optimizer [16] is used with default coefficients $\beta_1 = 0.9$ and $\beta_2 = 0.999$. For both the backbones, the total number of epochs is set to 140 and the batch size is set to 12 images per GPU card. The same learning rate schedule is used for both models. The learning rate is initially set to 0.001 and then decayed to 10^{-4} and 10^{-5} at the 90-th and 120-th epoch respectively. We use 4 and 8 V100 GPUs to accelerate the training for the two LOGO-CAP models with HRNet-W32 and HRNet-W48 respectively. The resolution of training images is 512×512 and 640×640 for the two models respectively. Following the widely adopted experimental settings in [37], the data augmentations in training include (1) random rotation with the rotation degree from -30° to 30° , (2) random scaling with the factor in the range of $[0.75, 1.5]$, (3) random translation in the range $[-40\text{pix}, 40\text{pix}]$ along both x and y directions, and (4) random horizontal flipping with the probability of 0.5.

Similarly, for different hyperparameters such as the trade-off parameter λ in the total loss, we did not run computationally expensive hyperparameter optimization for simplicity.

Testing. We focus on the single-scale testing protocol in the COCO keypoint benchmark for the sake of efficient human pose estimation. In the testing phase, the short side of input images is resized to a specific length (*e.g.*, 384, 512, or 640 pixels) and keep unchanged the aspect ratio between the height and the width. As commonly adopted in many bottom-up pose estimation approaches (*e.g.*, AE [22], HrHRNet [5], DEKR [11]), the flip testing is used as our default setting for the fair comparison. In the implementation, we feed the stacked tensor with an input image and a horizontally-flipped one together to get the global heatmaps and the offset fields. The flipped outputs are then averaged (according to the flip index) to get the final global heatmaps and the offset fields. For the computation of local heatmaps and the local-global adaptation, only the non-flipped outputs are used for the final predictions.

B Ablation Study

In this section, we run a series of experiments to verify the effectiveness of the design for our proposed Local-Global Contextual Adaptation module. We use HRNet-W32 as our backbone for all ablation studies with the training schedule described in Appendix A.

B.1 Effectiveness of the Different Components for Contextual Adaptation

We train 6 models to study the effectiveness in Table 5 for the used components: (1) OKS Loss for learning local KAMs, (2) the Gaussian Reweighting scheme and (3) the Attentive Norm for convolutional message passing. Compared with the center-offset baseline, the model (a) trained with OKS loss for the local KAMs estimation obtains a large improvement of AP by 6.1 points, justifying that the potential of using local KAMs for better pose estimation. For (b), we set the factor of OKS Loss to 0 and train the model by using the end-to-end reweighing scheme. In this setting, the local KAMs are learned only under the supervision of the contextual adaptation. Similar to model (a), a large improvement is also obtained compared against the baseline. Then, we train

HRNet-W32	OKS Loss	Reweigh	AttNorm	AP	AP ⁵⁰	AP ⁷⁵	AP ^M	AP ^L
baseline	-	-	-	60.0	84.4	66.4	54.0	71.1
(a)	✓	-	-	66.1	86.7	72.7	60.0	75.6
(b)	-	✓	-	67.6	87.0	74.3	62.1	76.7
(c)	✓	✓	-	69.0	87.0	75.2	63.4	77.5
(d)	✓	-	✓	65.8	86.8	72.3	59.3	75.4
(e)	-	✓	✓	67.5	86.6	74.1	62.2	76.7
(f)	✓	✓	✓	69.6	87.5	75.9	64.1	78.0

Table 5: Ablation studies on the three components of the Local-Global Contextual Adaptation module: the OKS loss, the Gaussian reweighing method for heatmaps and the Attentive Normalization.

size of local KEM	Message Passing	AP	AP50	AP75	APM	APL	FPS
7×7	3+1	68.4	86.6	74.9	63.4	76.6	21.8
11×11	1	68.8	86.9	74.9	63.1	77.5	22.5
11×11	3+1	69.6	87.5	75.9	64.1	78.0	20.7
15×15	3+1	69.3	87.1	75.2	63.2	78.3	16.5
19×19	3+1	69.0	87.1	75.2	62.8	78.2	13.2

Table 6: Ablation study of the different size of the local KEMs.

Type of the Prior	AP	AP50	AP75	APM	APL
KEMs only	59.4	80.8	62.8	50.9	71.6
KAMs only	65.7	86.0	72.3	60.6	74.0
LOGO-CAP (KEMs + KAMs)	69.6	87.5	75.9	64.1	78.0

Table 7: Ablation study of using different type of the priors for our LOGO-CAP. The KEMs and KAMs denote the global ones used for the adaptation.

the model (c) that uses both OKS loss and the reweighing scheme while replacing the AttNorm [19] to BatchNorm in the convolutional message passing module. It is shown that the OKS loss and the reweighing scheme collaborate very well with a further improvement obtained. For the effectiveness of AttNorm that exploits the feature recalibration mechanism for Neural Networks, it is shown in Table 5 (c-f) that the feature recalibration mechanism of AttNorm requires different information sources in human pose estimation. By enabling all the components, our LOGO-CAP-W32 finally obtains an AP of 69.6 on the COCO-val-2017 dataset.

B.2 Size of the Local KEMs and the Design of Convolutional Message Passing

We perform an ablation study with the results shown in Table 6, which confirms that the kernel size of 11×11 obtains the best performance. One possible explanation is that smaller kernel sizes fail to compensate the uncertainty of the initial keypoint estimation results, while larger kernel sizes may introduce more nuisances factors that affect the performance, such as the “collision” between different local KEMs of different keypoints from either the same person or adjacent different persons. Third, for different designs of the CMP module, we perform the ablation study for the different implementations. In detail, we replace the original architecture that is consist of 3 Conv+Normalization+ReLU layers and 1 output Conv layer (denoted by 3+1 in Table 6) to a simpler architecture that only use 1 output Conv layer (denoted by 1) for dimension reduction. It is shown that the 3+1 architecture performs better than the one only using the output Conv layer.

B.3 Different Type of the Priors for Contextual Adaptation

As our contextual adaptation takes both the global KEMs and KAMs as priors for final pose predictions, we quantitatively compare the possible designs for the contextual adaptation. In Table 7, we compare the performance on the COCO-val-2017 dataset by using either global KEMs or the learned global KAMs to the one that use two sources for prediction. On one hand, since the global KEMs are actually the standard Gaussian around each initial keypoint, it cannot provide more information

for refinement. On another hand, when we enforce the use of local KAMs for adaptation with only global KEMs, the uncertainty from local KEMs will affect the results. That is the reason why only using global KEMs is worse than using global KAMs. When using both global KEMs and KAMs, our approach obtains the best performance.

C The Computation of the Empirical Upper Bound

We elaborate on the details of computing the empirical upper bound of performance for a vanilla center-offset pose estimation method.

Network Architecture. The vanilla center-offset regression baseline uses the ImageNet pretrained HRNet-W32 [30] as the backbone, and the same modules as in our LOGO-CAP+HRNet-W32 for the center heatmap regression and the offset vector regression. See Fig. 3 and Section 3 for detailed specifications. We present the details of computing keypoint expansion maps (KEMs) that are used in calculating the empirical upper bound as follows.

Computation of Keypoint Expansion Maps. Denoted by $\mathcal{P}_{N \times 17 \times 2}$ the initial pose parameters (i.e., the 2-D locations for the 17 keypoints of the N pose instances) estimated by the vanilla center-offset method, we expand each of the estimated keypoints with a local 11×11 mesh grid, that is to lift a keypoint to a 2-D mesh to counter the estimation uncertainty. As shown in the Alg. 1, we use the COCO benchmark provided keypoint sigmas to scale the unit length of the meshgrid for different types (e.g., nose, eyes, hips) of keypoints. After getting the expanded keypoint meshes \mathcal{M} of the initial poses, we compute their keypoint similarities $\mathcal{S}_{N \times 11 \times 11 \times K \times 17}$ between the groundtruth keypoints $\mathcal{G}_{K \times 17 \times 3}$ and the keypoint expansion maps. After applying the sum reduction on the similarity tensor $\mathcal{S}_{N \times 11 \times 11 \times K \times 17}$ along the 2-nd, 3-rd and the last axes, we have known the optimal correspondence (including the low-quality matches) for each center anchor, denoted by $\mathcal{S}_{N \times 11 \times 11 \times 17}$. Then, the pose with the maximal similarity in the 11×11 local window for each center anchor are used as the best one to compute the empirical upper bound on the fully-annotated COCO-val-2017 dataset.

Algorithm 1: Computation of Keypoint Expansion Maps in a PyTorch-like style

```

1 coco_sigmas = torch.tensor([0.026, 0.025, 0.025, 0.035, 0.035, 0.079, 0.079, 0.072, 0.072,
    0.062, 0.062, 0.107, 0.107, 0.087, 0.087, 0.089, 0.089 ]) #Keypoint sigmas for the
    COCO dataset.
2 def KptsExpansionCoco( $\mathcal{P}$ , ksize=11)
    #Initial poses  $\mathcal{P}$ :  $N \times 17 \times 2$ 
3     radius = ksize // 2
4     dy, dx = torch.meshgrid(torch.arange(-radius, radius), torch.arange(-radius, radius))
    #dx, dy:  $ksize \times ksize$ 
5     dy, dx = dy.reshape(1, 1, ksize, ksize), dx.reshape(1, 1, ksize, ksize)
6     scale = coco_sigmas.reshape(1, 17, 1, 1) / coco_sigmas.min() #using different
    expansion rate for the different keypoint categories.
7     dy = dy * scale #dy:  $1 \times 17 \times 11 \times 11$ 
8     dx = dx * scale #dx:  $1 \times 17 \times 11 \times 11$ 
9     dxy = torch.stack((dx, dy), dim=-1) #dxy:  $1 \times 17 \times 11 \times 11 \times 2$ 
10     $\mathcal{M} = \mathcal{P}.reshape(N, 17, 1, 1, 2) + dxy$  # $\mathcal{M}$ :  $N \times 17 \times 11 \times 11 \times 2$ 
11    return  $\mathcal{M}$ 

```

D Inference Speed

D.1 The Speed-Accuracy Comparisons

We elaborate on the speed-accuracy comparisons in Fig 2, which is reproduced in Fig. 5.

We compare our LOGO-CAP with state-of-the-art bottom-up pose estimation approaches in terms of the speed-accuracy trade-off using different input resolutions of testing images.

- Both the proposed LOGO-CAP method and the DEKR [11] method have two versions of models trained with the HRNet-W32 backbone at the resolution of 512×512 , and the HRNet-W48 backbone at the resolution of 640×640 , respectively. The two versions of models are denoted by $W32$ and $W48$ respectively in Fig. 5. In comparing the speed-accuracy trade-offs, we evaluate each of the two versions of models with two different resolutions: For $W32$, we test the models, LOGO-CAP and DEKR, under the resolutions of 384 and 512 for short side of the testing images, which are denoted by $W32 - 384$ and $W32 - 512$ in Fig. 5 respectively. Similarly, it is done for the $W48$ models. The longer side of the testing images are computed according to their original aspect ratios.
- For the CenterNet method [39], we report the result obtained using the large Hourglass backbone [23] due to its better AP score. The testing resolution is 512 in the short side of the images.
- For the PifPaf method [17], we report their results using three different backbones of ResNet-50, ResNet-101 and ResNet-152 [13]. We follow the image resolution setting presented in the original paper [17] that resizes the long side of the testing images to be 641 and keep the original aspect ratio.
- For the associative embedding approach [22], the result using the Higher-HRNet-W32 [5] as the backbone is reported for the concern of inference speed. The testing resolution is also 512 in the short side of the testing image.

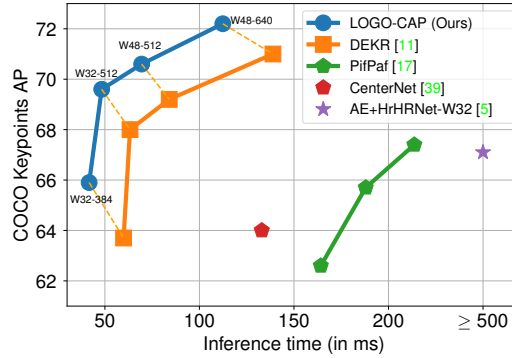


Figure 5: Speed-accuracy comparisons between our LOGO-CAP and prior arts on the COCO val-2017 dataset. $Wx-Y$ (e.g. $W32-384$) means that a model uses the backbone HRNet- Wx (HRNet-W32) and is tested with the image resolution Y in the short side.

As shown in Fig. 5, our approach obtains the best speed-accuracy trade-off with different backbones and image resolutions. When using HRNet-W32 as the backbone, our LOGO-CAP uses the low-resolution images (with 384 pixels in the short side) obtains the AP of 65.9 while approaching real-time performance with the FPS of 24.0, which surpasses DEKR [11] by 2.2 AP and 7.3 FPS. Benefitting from our design rationales of simplicity and fully end-to-end learning, our approach also obtains the best performance in both aspects of speed and accuracy when increasing the image resolution to 512 and 640.

D.2 The Breakdown of Inference Time

Here, we analyze the inference time for different number of persons in the input image. As shown in Table 8, the main bottleneck of the inference time is the backbone. For the Local-Global Contextual Adaptation module, it only takes about 10 ms on average.

E More Qualitative Results

Results on the COCO-val-2017 and the OCHuman Datasets. Fig. 6 shows examples of pose estimation in the two datasets by the proposed LOGO-CAP with the HRNet-W32 backbone. Our proposed LOGO-CAP is able to handle large structural and appearance variations in human pose estimation.

	Numer of Persons	Backbone	Local KEMs	Local KAMs	Global KAMs
LOGO-CAP (W32)	-	38.6 ms	3.05 ms	2.49 ms	2.85 ms
	1		2.39 ms	1.14 ms	1.12 ms
	30		3.69 ms	3.49 ms	5.87 ms
LOGO-CAP (W48)	-	99.9 ms	4.18 ms	3.00 ms	3.34 ms
	1		3.19 ms	1.10 ms	1.07 ms
	30		2.97 ms	3.59 ms	5.97 ms

Table 8: The breakdown of inference time of the proposed LOGO-CAP method. The inference time is averagely computed using a NVIDIA TITAN RTX GPU on the COCO-val-2017 dataset. For each model, we seperately report the averaged inference time across 5000 images, the averaged inference time in the images that detect only one person, the avaraged inference time in the images that have 30 persons.



Figure 6: Qualitative results of our LOGO-CAP (HRNet-W32). All images were picked thematically without considering our algorithms performance. The first three rows display our approach on the COCO-val-2017 dataset and the last three ones show our results on the OCHuman test dataset.

Fast pose estimation for video frames. To justify the potential of our proposed approach in practical applications, we run our LOGO-CAP (W32 model) on two videos that have the resolution of 1280×720 from YouTube. We follow our testing protocol to resize the short side of the video frames to 512 pixels and keep their original aspect ratios for inference. Without using any pose tracking techniques, our LOGO-CAP achieves fast and accurate human pose estimation. Please click the following google drive links for the demo videos:

- <https://bit.ly/3z2t8fA> (video credit: <https://youtu.be/2DiQUX11YaY>)
- <https://bit.ly/3cghWT4> (video credit: <https://youtu.be/kTvzU1sGSyA>)

In these two demo videos, the instantaneous FPS for each video frame is marked in the left corner of the video.

References

- [1] Mykhaylo Andriluka, Stefan Roth, and Bernt Schiele. Pictorial structures revisited: People detection and articulated pose estimation. In *2009 IEEE conference on computer vision and pattern recognition*, pages 1014–1021. IEEE, 2009. 3
- [2] Richard Bellman. Dynamic programming. *Science*, 153(3731):34–37, 1966. 3
- [3] Zhe Cao, Gines Hidalgo Martinez, Tomas Simon, Shih-En Wei, and Yaser A. Sheikh. Openpose: Realtime multi-person 2d pose estimation using part affinity fields. *IEEE Trans. on Pattern Analysis and Machine Intelligence (PAMI)*, 2019. 1, 2, 3, 8
- [4] Zhe Cao, Tomas Simon, Shih-En Wei, and Yaser Sheikh. Realtime multi-person 2d pose estimation using part affinity fields. In *IEEE Conference on Computer Vision and Pattern Recognition (CVPR)*, pages 1302–1310, 2017. 3
- [5] Bowen Cheng, Bin Xiao, Jingdong Wang, Honghui Shi, Thomas S. Huang, and Lei Zhang. Higherhrnet: Scale-aware representation learning for bottom-up human pose estimation. In *IEEE/CVF Conference on Computer Vision and Pattern Recognition (CVPR)*, pages 5385–5394. IEEE, 2020. 3, 8, 9, 10, 13
- [6] Kaiwen Duan, Song Bai, Lingxi Xie, Honggang Qi, Qingming Huang, and Qi Tian. Centernet: Keypoint triplets for object detection. In *IEEE/CVF International Conference on Computer Vision (ICCV)*, pages 6568–6577, 2019. 2, 4
- [7] Haoshu Fang, Shuqin Xie, Yu-Wing Tai, and Cewu Lu. RMPE: regional multi-person pose estimation. In *IEEE International Conference on Computer Vision (ICCV)*, pages 2353–2362, 2017. 9
- [8] Pedro F Felzenszwalb and Daniel P Huttenlocher. Pictorial structures for object recognition. *International journal of computer vision*, 61(1):55–79, 2005. 3
- [9] Pedro F Felzenszwalb and Ramin Zabih. Dynamic programming and graph algorithms in computer vision. *IEEE transactions on pattern analysis and machine intelligence*, 33(4):721–740, 2010. 3
- [10] Martin A Fischler and Robert A Elschlager. The representation and matching of pictorial structures. *IEEE Transactions on computers*, 100(1):67–92, 1973. 3
- [11] Zigang Geng, Ke Sun, Bin Xiao, Zhaoxiang Zhang, and Jingdong Wang. Bottom-up human pose estimation via disentangled keypoint regression. In *IEEE Conference on Computer Vision and Pattern Recognition (CVPR)*, 2021. 1, 2, 3, 4, 8, 9, 10, 13
- [12] Kaiming He, Georgia Gkioxari, Piotr Dollár, and Ross B. Girshick. Mask R-CNN. In *IEEE International Conference on Computer Vision (ICCV)*, pages 2980–2988, 2017. 1, 2
- [13] Kaiming He, Xiangyu Zhang, Shaoqing Ren, and Jian Sun. Deep residual learning for image recognition. In *IEEE Conference on Computer Vision and Pattern Recognition (CVPR)*, pages 770–778, 2016. 13
- [14] Sheng Jin, Wentao Liu, Enze Xie, Wenhai Wang, Chen Qian, Wanli Ouyang, and Ping Luo. Differentiable hierarchical graph grouping for multi-person pose estimation. In *European Conference on Computer Vision (ECCV)*, volume 12352, pages 718–734, 2020. 3, 8
- [15] Daniel Kahneman. *Thinking, fast and slow*. Macmillan, 2011. 2

- [16] Diederik P. Kingma and Jimmy Ba. Adam: A method for stochastic optimization. In Yoshua Bengio and Yann LeCun, editors, *International Conference on Learning Representations (ICLR)*, 2015. 10
- [17] Sven Kreiss, Lorenzo Bertoni, and Alexandre Alahi. Pifpaf: Composite fields for human pose estimation. In *IEEE Conference on Computer Vision and Pattern Recognition (CVPR)*, pages 11977–11986, 2019. 1, 3, 8, 9, 13
- [18] Jia Li, Wen Su, and Zengfu Wang. Simple pose: Rethinking and improving a bottom-up approach for multi-person pose estimation. In *AAAI Conference on Artificial Intelligence (AAAI)*, pages 11354–11361, 2020. 8
- [19] Xilai Li, Wei Sun, and Tianfu Wu. Attentive normalization. In Andrea Vedaldi, Horst Bischof, Thomas Brox, and Jan-Michael Frahm, editors, *European Conference on Computer Vision (ECCV)*, volume 12362, pages 70–87, 2020. 6, 11
- [20] Tsung-Yi Lin, Michael Maire, Serge J. Belongie, James Hays, Pietro Perona, Deva Ramanan, Piotr Dollár, and C. Lawrence Zitnick. Microsoft COCO: common objects in context. In David J. Fleet, Tomás Pajdla, Bernt Schiele, and Tinne Tuytelaars, editors, *European Conference on Computer Vision (ECCV)*, volume 8693, pages 740–755, 2014. 7, 10
- [21] Kevin Murphy, Yair Weiss, and Michael I Jordan. Loopy belief propagation for approximate inference: An empirical study. *arXiv preprint arXiv:1301.6725*, 2013. 3
- [22] Alejandro Newell, Zhiao Huang, and Jia Deng. Associative embedding: End-to-end learning for joint detection and grouping. In *Advances in Neural Information Processing Systems 30 (NeurIPS)*, pages 2277–2287, 2017. 3, 4, 8, 9, 10, 13
- [23] Alejandro Newell, Kaiyu Yang, and Jia Deng. Stacked hourglass networks for human pose estimation. In *European Conference on Computer Vision (ECCV)*, pages 483–499, 2016. 13
- [24] Xuecheng Nie, Jiashi Feng, Jianfeng Zhang, and Shuicheng Yan. Single-stage multi-person pose machines. In *IEEE/CVF International Conference on Computer Vision (ICCV)*, pages 6950–6959, 2019. 8
- [25] George Papandreou, Tyler Zhu, Liang-Chieh Chen, Spyros Gidaris, Jonathan Tompson, and Kevin Murphy. Personlab: Person pose estimation and instance segmentation with a bottom-up, part-based, geometric embedding model. In *European Conference on Computer Vision (ECCV)*, pages 282–299, 2018. 1, 3, 8
- [26] Leonid Pishchulin, Mykhaylo Andriluka, Peter Gehler, and Bernt Schiele. Poselet conditioned pictorial structures. In *Proceedings of the IEEE Conference on Computer Vision and Pattern Recognition*, pages 588–595, 2013. 3
- [27] Deva Ramanan, David A Forsyth, and Andrew Zisserman. Strike a pose: Tracking people by finding stylized poses. In *2005 IEEE Computer Society Conference on Computer Vision and Pattern Recognition (CVPR’05)*, volume 1, pages 271–278. IEEE, 2005. 3
- [28] Brandon Rothrock, Seyoung Park, and Song-Chun Zhu. Integrating grammar and segmentation for human pose estimation. In *Proceedings of the IEEE Conference on Computer Vision and Pattern Recognition*, pages 3214–3221, 2013. 3
- [29] Ke Sun, Zigang Geng, Depu Meng, Bin Xiao, Dong Liu, Zhaoxiang Zhang, and Jingdong Wang. Bottom-up human pose estimation by ranking heatmap-guided adaptive keypoint estimates. *CoRR*, abs/2006.15480, 2020. 2, 4
- [30] Ke Sun, Bin Xiao, Dong Liu, and Jingdong Wang. Deep high-resolution representation learning for human pose estimation. In *IEEE Conference on Computer Vision and Pattern Recognition (CVPR)*, pages 5693–5703, 2019. 2, 5, 10, 12
- [31] Zhi Tian, Hao Chen, and Chunhua Shen. Directpose: Direct end-to-end multi-person pose estimation. *CoRR*, abs/1911.07451, 2019. 2, 4
- [32] Zhi Tian, Chunhua Shen, Hao Chen, and Tong He. FCOS: fully convolutional one-stage object detection. In *IEEE/CVF International Conference on Computer Vision (ICCV)*, pages 9626–9635, 2019. 4
- [33] Ali Varamesh and Tinne Tuytelaars. Mixture dense regression for object detection and human pose estimation. In *IEEE/CVF International Conference on Computer Vision and Pattern Recognition (CVPR)*, pages 13083–13092, 2020. 4

- [34] Ashish Vaswani, Noam Shazeer, Niki Parmar, Jakob Uszkoreit, Llion Jones, Aidan N Gomez, Lukasz Kaiser, and Illia Polosukhin. Attention is all you need. *arXiv preprint arXiv:1706.03762*, 2017. 9
- [35] Bin Xiao, Haiping Wu, and Yichen Wei. Simple Baselines for Human Pose Estimation and Tracking. *Computer Vision and Pattern Recognition*, 2018. 9
- [36] Yi Yang and Deva Ramanan. Articulated human detection with flexible mixtures of parts. *IEEE transactions on pattern analysis and machine intelligence*, 35(12):2878–2890, 2012. 3
- [37] Feng Zhang, Xiatian Zhu, Hanbin Dai, Mao Ye, and Ce Zhu. Distribution-aware coordinate representation for human pose estimation. In *IEEE/CVF Conference on Computer Vision and Pattern Recognition (CVPR)*, pages 7091–7100, 2020. 10
- [38] Song-Hai Zhang, Ruilong Li, Xin Dong, Paul L. Rosin, Zixi Cai, Xi Han, Dingcheng Yang, Haozhi Huang, and Shi-Min Hu. Pose2seg: Detection free human instance segmentation. In *IEEE Conference on Computer Vision and Pattern Recognition (CVPR)*, pages 889–898, 2019. 7, 9
- [39] Xingyi Zhou, Dequan Wang, and Philipp Krähenbühl. Objects as points. *CoRR*, abs/1904.07850, 2019. 2, 3, 4, 8, 9, 13